atmosphere

MDPI

Article

Evolution of Atmospheric Carbon Dioxide and Methane Mole Fractions in the Yangtze River Delta, China

Kai Jiang [1,2], Qianli Ma [3,*], Kunpeng Zang [1,2], Yi Lin [1,2], Yuanyuan Chen [1,2], Shuo Liu [1,2], Xuemei Qing [1,2], Shanshan Qiu [1,2], Haoyu Xiong [1,2], Haixiang Hong [1,2], Jiaxin Li [1,2] and Shuangxi Fang [2,4,*]

1 College of Environment, Zhejiang University of Technology, Hangzhou 310014, China
2 Zhejiang Carbon Neutral Innovation Institute, Zhejiang University of Technology, Hangzhou 310014, China
3 Lin'an Regional Background Station, China Meteorological Administration, Hangzhou 311307, China
4 Yangtze River Delta R&D Centre, Monitoring & Assessment Center for GHGs & Carbon Neutrality, China Meteorological Administration, Beijing 100081, China
* Correspondence: wingedsteed@me.com (Q.M.); fangsx@zjut.edu.cn (S.F.)

Abstract: As the most economically developed region in China, the Yangtze River Delta (YRD) region contributed to ~17% of the total anthropogenic CO_2 emissions from China. However, the studies of atmospheric CO_2 and CH_4 in this area are relatively sparse and unsystematic. Here, we analyze the changing characters of those gases in different development periods of China, based on the 11-year atmospheric CO_2 and CH_4 records (from 2010 to 2020) at one of the four Chinese sites participating in the World Meteorological Organization/Global Atmospheric Watch (WMO/GAW) program (Lin'an regional background station), located in the center of YRD region, China. The annual average atmospheric CO_2 and CH_4 mole fractions at LAN have been increasing continuously, with growth rates of 2.57 ± 0.14 ppm yr^{-1} and 10.3 ± 1.3 ppb yr^{-1}, respectively. Due to the complex influence of regional sources and sinks, the characteristics of atmospheric CO_2 and CH_4 varied in different periods: (i) The diurnal and seasonal variations of both CO_2 and CH_4 in different periods were overall similar, but the amplitudes were different. (ii) The elevated mole fractions in all wind sectors tended to be uniform. (iii) The potential source regions of both gases expanded over time. (iv) The growth rate in recent years (2016–2020) changed significantly less than that in the earlier period (2010–2015). Our results indicated that the CO_2 and CH_4 mole fractions were mainly correlated to the regional economic development, despite the influence of special events such as the G20 Summit and COVID-19 lockdown.

Keywords: carbon dioxide; methane; variation; mole fraction; evolution

Citation: Jiang, K.; Ma, Q.; Zang, K.; Lin, Y.; Chen, Y.; Liu, S.; Qing, X.; Qiu, S.; Xiong, H.; Hong, H.; et al. Evolution of Atmospheric Carbon Dioxide and Methane Mole Fractions in the Yangtze River Delta, China. *Atmosphere* **2023**, *14*, 1295. https://doi.org/10.3390/atmos14081295

Academic Editor: James Lee

Received: 20 June 2023
Revised: 30 July 2023
Accepted: 10 August 2023
Published: 16 August 2023

1. Introduction

Carbon dioxide (CO_2) and methane (CH_4) are the main greenhouse gases (GHGs) that contribute approximately 66% and 16%, respectively, of the total radiation forcing among all the long-lived greenhouse gases [1,2]. Due to the influence of human activities since the industrial revolution era, increasing atmospheric greenhouse gases have caused serious climate change, which has exerted a huge impact on the economy, society, ecology, and other aspects [3]. Since the pre-industrial era, atmospheric CO_2 has increased rapidly, rising by about 2~3 ppm per year from 2010 to 2020 [2]. Similarly, the global average CH_4 mole fraction reached a new height of 1889 ± 2 ppb in 2020, with a higher annual growth rate (12.0 ppb yr^{-1}) than the average over the past decade (8.0 ppb yr^{-1}), and it has become the fastest growing greenhouse gas [2].

Atmospheric CO_2 is mainly emitted from anthropogenic sources (e.g., respiration, fossil fuel, and biomass burning) [4]. Marine and terrestrial ecosystems are the major sinks of atmospheric CO_2, absorbing about half of the anthropogenic emissions, and the net absorption has been increasing over the past 50 years [5–7]. Combined with the influence of various transport processes, the source and sink distribution of global atmospheric CO_2

is patchy and has obvious spatial and temporal variations [8]. As for CH_4, natural sources including ruminants and wetlands account for 40%, while anthropogenic sources including paddies, cattle ranch, fossil fuel, and biomass burning account for 60% [9–12]. Wetland emissions dominate the interannual variation of methane sources, while fire emissions play a minor role, except during El Niño [13–15]. The destruction of CH_4 by hydroxyl radicals in the troposphere is the main sink, accounting for 90% of the total loss [16].

Because of the massive increase in fossil fuel consumption in recent decades, China has become the world's largest emitter of greenhouse gases [17,18]. However, China started relatively late in greenhouse gas background observation, and in situ atmospheric CO_2 and CH_4 observations were not conducted until 1994 at Mount. Waliguan (WLG) Station in Qinghai Province. Liu et al. [19] found that atmospheric CH_4 at the WLG station increased at an average annual growth rate of 5.1 ± 0.1 ppb yr^{-1} from 1994 to 2019, but it was close to zero or negative in some specific periods. Fang et al. [20] analyzed the trends of CO_2 and CH_4 at Shangdianzi (SDZ) regional station in China from 2009 to 2013. Because of the strong anthropogenic emissions from Beijing-Tianjin-Hebei (BTH), the mole fractions and annual growth rates for CO_2 and CH_4 at SDZ were distinctly higher. At Longfengshan (LFS) regional station, the CO_2 and CH_4 mole fractions displayed increasing trends in 2009–2013, with a growth rate of 3.1 ± 0.02 ppm yr^{-1} for CO_2 and 8 ± 0.04 ppb yr^{-1} for CH_4 [21].

The Yangtze River Delta (YRD), which includes Jiangsu Province, Zhejiang Province, Anhui Province, and Shanghai, is one of China's most developed regions and one of the world's largest greenhouse gas emitters [22–25]. The reported CO_2 emissions in this region accounted for about 17% of the total anthropogenic emissions in China in 2017 [26]. To understand the characteristics and the abundance of greenhouse gases in this region, the Chinese Meteorological Administration (CMA) established the Lin'an (LAN) station in the center of the Yangtze River Delta in 1983. The station is marked as a regional weather station by the World Meteorological Organization/Global Atmospheric Watch (WMO/GAW). There was no in situ CO_2 and CH_4 measuring system at LAN prior to the installation of a cavity ring-down spectrometer (G1301, Picarro Inc., Santa Clara, CA, USA) in January 2009. The long-term observation of atmospheric background CO_2 and CH_4 provides a scientific understanding of the CO_2 and CH_4 source/sink characteristics in YRD.

This study presents almost 11-year (from 2010 to 2020) ground-based observations of CO_2 and CH_4 at the LAN background station in the YRD region. We analyze the evolution characteristics and temporal-spatial distributions of the background CO_2 and CH_4 at the site, which can be used to study the evolution of atmospheric greenhouse gases in eastern China. In September 2020, China announced a new goal of "striving to achieve a carbon peak by 2030 and achieve carbon neutrality by 2060" to tackle climate change. This study provides a scientific basis for evaluating the effectiveness of greenhouse gas management and emission control policies.

2. Methodology

2.1. Sampling Site

Lin'an (LAN) station (30°18′ N, 119°44′ E, 138.6 m a.s.l.), is one of the seven regional atmospheric background stations operated by the CMA and also a member station of the WMO/GAW program. The LAN station is located about 50 km west of Hangzhou (the capital city of Zhejiang Province in China) and 150 km southwest of Shanghai (Figure 1). North of the LAN station (1.4 km away) is a small factory that produces charcoal from bamboo wood. The southwest and southeast of LAN are Lin'an Town and Qingshan Lake, respectively. The observatory is on the top of a small hill with dense vegetation coverage, surrounded by hilly lands and farming areas. The station is located in the humid subtropical monsoon climate zone, with an average annual precipitation of 1480 mm and an average temperature of 15.3 °C [27]. The wind directions of the LAN station were mainly northeast and southwest accounting for 29.2% and 22.6%, respectively, and the frequency of calm wind was 4% [25].

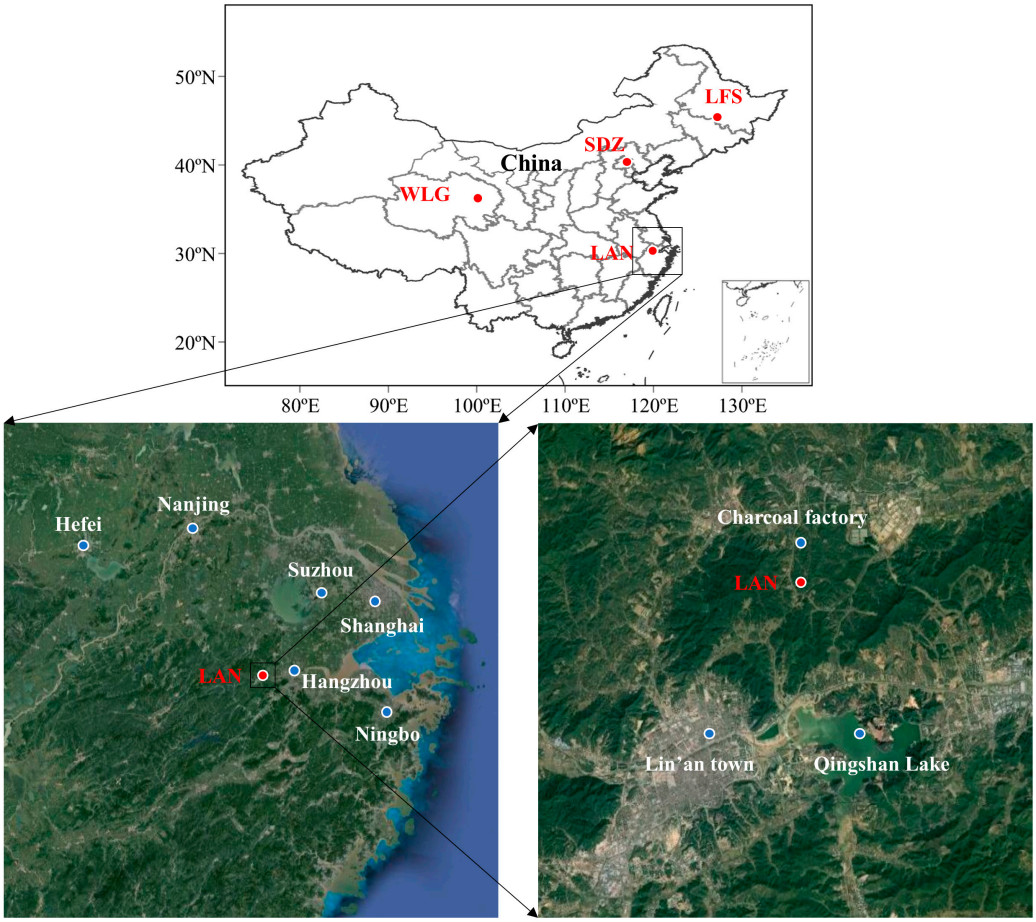

Figure 1. Location of the LAN regional station. The red dots represent the LAN station and three other background station (WLG, SDZ and LFS) in China. The blue dots represent the cities or towns near the station. The China map was derived from the © National Geomatics Center of China (http://www.ngcc.cn/ngcc/, accessed on 20 November 2022). The satellite maps were derived from the © Google Maps (http://www.google.com/maps, last access: 10 January 2022).

2.2. Instrumental Set-Up

The CO_2 and CH_4 mole fractions are continuously observed by a CRDS analyzer set up on 1 January 2009, which has been proven to be extremely suitable for accurate measurement, as the analyzer's responses to CO_2 and CH_4 are highly linear and stable [28,29]. The instrument was initially G1301 (Picarro Inc., USA) and was upgraded to G2401 (Picarro Inc., USA) in 2014. The air first passed through the filter screen by a vacuum pump (N022, KNF Neuberger, Freiburg-Munzingen, Germany) into a dedicated 10 mm o.d. sampling line. Then the air sample passed through a pressure releaser set at 1 atm gauge pressure to release excess air pressure. The ambient air was dried to a dew point of about −60 °C through a glass cold trap soaked in an ethanol bath of −70 °C. The VICI 8-port sample selection valve was used to select ambient air or standard gas (T, WH, WL) for the subsequent process. The detailed process of the observation system was described by Fang et al. [30]. Throughout the system, the residence time of the air sample from the top of the inlet to the CRDs analyzer was less than 30 s.

Two standards were used to calculate the CO_2 and CH_4 mole fractions. Linear two-point fitting (WH and WL) was used to calibrate environmental measurements from the latest Standard Gas Measurements. The CO_2 and CH_4 measurements were correlated with the WMO CO_2 X2019 and WMO CH_4 X2004A scales, respectively. In addition, the precision and stability of the system were checked periodically with the target gas (T). The system analyzed the two standards and the target gas every 12 h. After calculating the mole

fractions, the data were manually examined to flag any analysis or sampling problems, which were then averaged into hourly segments for further processing and analysis. In this study, CO_2 and CH_4 were given as atmospheric mole fractions in dry air.

2.3. Data Processing

The observations of atmospheric CO_2 and CH_4 were inevitably affected by complex conditions such as local sources, transportation, and terrain change. Therefore, the records were not fully representative of well-mixed regional atmospheric CO_2 and CH_4 [31]. To obtain regionally representative data, we filtered the CO_2 and CH_4 data affected by local sources near the site, such as towns, factories, and farmlands. The hourly CO_2 and CH_4 data were divided into local and regional representativeness according to essential meteorological information [27]. In this study, the CO_2 records from these wind directions (including NE-ENE, SSW-SW, NW in spring, SSW, W-WNW-NW-NNW in summer, SE-SSE-S-SSW-SW-WSW in autumn, and NE-ENE-E-ESE-SE, WNW in winter), were flagged as locally influenced. Similarly, the CH_4 records from these wind directions (including NNE-NE-ENE-E-ESE in spring, N-NNE-NE-ENE-E in summer, NE-ENE-E, SE, W-WNW in autumn, and ENE-E-ESE-SE, WNW in winter), were flagged as locally influenced (31.79% for CO_2 and 34.72% for CH_4). Whereafter, we chose the period of a day when the atmospheric boundary layer was high and the vertical mixing was fast and uniform, e.g., 10:00–16:00 local time (LT) for both CO_2 and CH_4 data. The rest were flagged as locally influenced (47.80% for CO_2 and 47.04% for CH_4). Finally, we filtered the CO_2 and CH_4 data for surface wind speeds less than 1.5 m s^{-1} to local effects to minimize local accumulation (4.10% for CO_2 and 3.90% for CH_4).

In order to study the pollution transport path of air masses at LAN, the Hybrid Single-Particle Lagrangian Integrated Trajectory (HYSPLIT) diffusion model was used, based on the strength of gridded meteorological data (GDAS 1° data, 2010–2020) from the National Oceanographic and Atmospheric Administration's Air Resources Laboratory (NOAA ARL). We computed the 72 h back trajectories with 500 m a.g.l. for the hourly CO_2 and CH_4 mole fractions. We calculated the trajectories for January, April, July, and October, representing winter, spring, summer, and autumn, respectively. Based on the potential source contribution function (PSCF) method, the conditional probability that the residence times of air parcels with concentrations greater than the threshold would transport to the exact acceptor location was calculated. Then, the annual spatial source distributions of CO_2 and CH_4 were analyzed [32]. In this study, the PSCF value was calculated in $0.5 \times 0.5°$ grid cell (i, j) as follows:

$$\mathrm{PSCF}_{ij} = \mathrm{m}_{ij}/\mathrm{n}_{ij} \quad (1)$$

n_{ij} represents the number of endpoints that terminate in the $i\,j$ th grid cell, and m_{ij} represents the number of trajectories where the concentration exceeded the threshold value [33]. In order to reduce the abnormal effect of small n_{ij} values in some grid cells, PSCF_{ij} was further calculated by an arbitrary weighting function W_{ij} as follows:

$$\mathrm{W}_{ij} = \begin{cases} 1.00 & 3\mathrm{n}_{\mathrm{ave}} < \mathrm{n}_{ij} \\ 0.70 & 1.5\mathrm{n}_{\mathrm{ave}} < \mathrm{n}_{ij} \le 3\mathrm{n}_{\mathrm{ave}} \\ 0.42 & \mathrm{n}_{\mathrm{ave}} < \mathrm{n}_{ij} \le 1.5\mathrm{n}_{\mathrm{ave}} \\ 0.05 & \mathrm{n}_{ij} \le \mathrm{n}_{\mathrm{ave}} \end{cases} \quad (2)$$

W_{ij} represents the weight of cell (i, j), n_{ij} represents the number of trajectory endpoints falling in the $i\,j$ th grid cell, and the $\mathrm{n}_{\mathrm{ave}}$ represents the average of the endpoints in all grid cells.

To fill in the data gaps, we used the curve-fitting method of Thoning et al. [34] to assess the long-term trends of CO_2 and CH_4. We also calculated the trend curve without seasonal variation and then used the average of the first derivative of the trend curve to find the annual growth rate. The function is as follows:

$$f(t) = a_0 + a_1 t + a_2 t^2 + \cdots + a_{(k-1)} t^{(k-1)} + \sum_{n=1}^{nh} c_n [\sin(2n\pi t) + \varphi_n] \quad (3)$$

k represents the number of polynomial parts, and nh represents the number of harmonics parts. In this study, we applied k = 3 polynomial terms (quadratic terms) to the multiyear trends and nh = 4 annual harmonics to the seasonal cycles.

In addition, we also analyzed the interannual variation of CO_2 and CH_4 in different periods from 2010 to 2020. According to the important phases or critical periods of atmospheric CO_2 and CH_4 changes in previous studies (e.g., sharp changes in growth rates and mole fractions in 2012, the impact of the Hangzhou G20 Summit in 2016, and COVID-19 epidemic in 2020), the leap years were taken as the time nodes and the whole time series was divided into three observation periods, i.e., 2010–2012, 2013–2016, 2017–2020 [2,25,30,35].

3. Results and Discussions

3.1. Extracting the Regional Atmospheric CO_2 and CH_4

To accurately understand the variation of atmospheric CO_2 and CH_4 on a regional scale, it is essential to identify CO_2 and CH_4 records influenced by local pollutants [31]. The filtered regional or local time series is shown in Figure 2. In this study, 83.69% of CO_2 data and 85.66% of CH_4 data were classified as locally representative, indicating that the majority of the observed CO_2 and CH_4 records were influenced by very local sources and sinks (e.g., factory, town), albeit the station was installed as a regional background station in 1983. The urbanization in the east of China, as the most economically developed region in the country, had a distinct influence on the atmospheric greenhouse gas mole fractions. The mean CO_2 and CH_4 values affected by the local area were 424.66 $\pm$ 0.13 ppm and 2051.8 $\pm$ 0.8 ppb, respectively, which were both higher than the regional representative values (415.31 $\pm$ 0.26 ppm and 2007.3 $\pm$ 1.6 ppb). As shown in Figure 3, the annual mean mole fractions of CO_2 and CH_4 have increased from 400.72 $\pm$ 0.73 ppm and 1949.9 $\pm$ 6.0 ppb in 2010 to 427.73 $\pm$ 0.65 ppm and 2035.1 $\pm$ 4.7 ppb in 2020, with an annual mean increase of 2.70 ppm and 8.5 ppb, respectively. Compared with the Marine Boundary Layer reference surface values (30° N) of CO_2 and CH_4 in 2020 (414.62 ppm for CO_2 and 1932.4 ppb for CH_4) (https://gml.noaa.gov/ccgg/mbl/mbl.html, accessed on 31 May 2022), the atmospheric CO_2 and CH_4 mole fractions at the LAN station were 13.11 ppm and 102.7 ppb higher, respectively. These results indicated that the YRD region in China was acting as a strong source of atmospheric CO_2 and CH_4 in recent years [36,37].

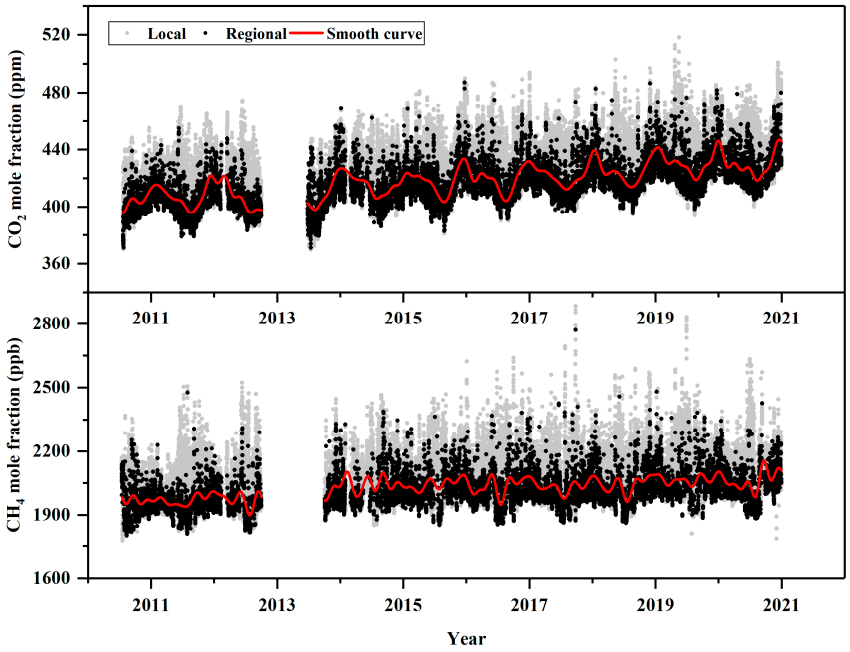

Figure 2. The filtered hourly CO_2 and CH_4 times series observed at the LAN station from 2010 to 2020. The grey points denote locally influenced data and the black points denote regionally representative data. The red lines are the smooth curves of the regional data obtained by the curve-fitting program [34]. There are data gaps caused by the malfunction of the instrument from 1 October 2012 to 26 June 2013 for CO_2 and from 1 October 2012 to 3 October 2013 for CH_4.

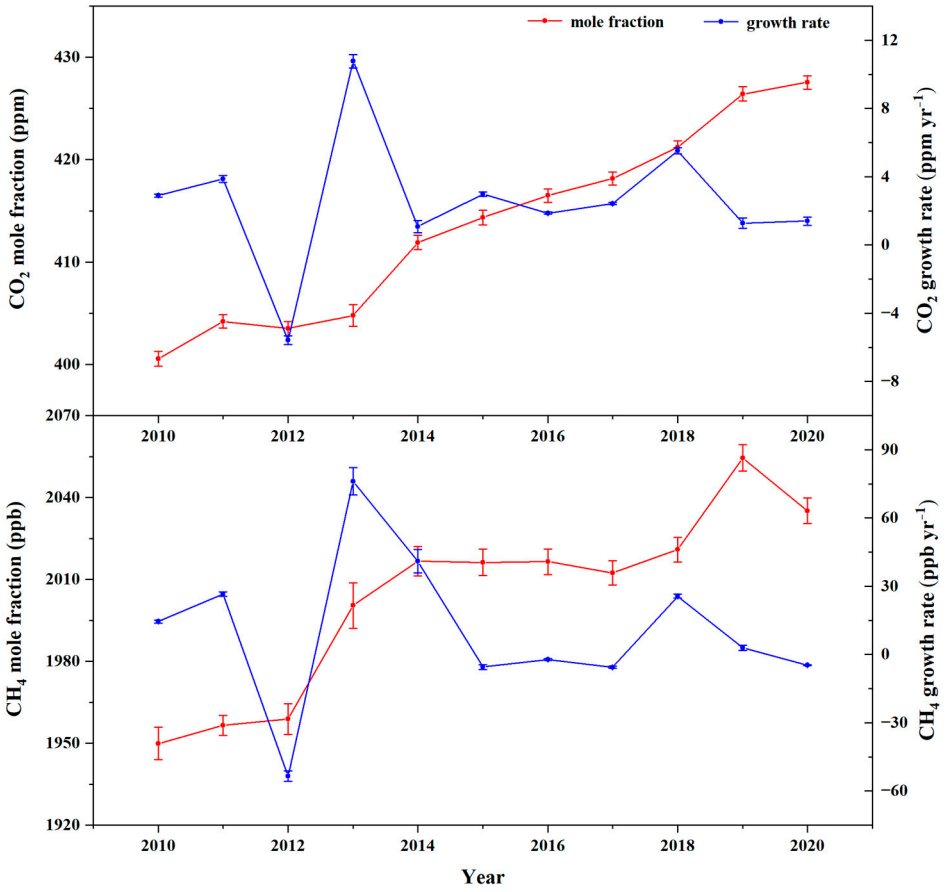

Figure 3. The yearly average CO_2 and CH_4 mole fractions and growth rates at the LAN station from 2010 to 2020. Error bars indicate 95% confidence intervals.

3.2. Diurnal Variations

As shown in Figure 4, distinct diurnal variations were observed in four seasons during 2010–2020 at LAN. The diurnal variations of CO_2 and CH_4 mole fractions were similar, i.e., reaching the maximum value in the morning, decreasing, appearing to trough in the afternoon, and gradually increasing in the evening. These diurnal variations were closely related to plant photosynthesis, biological respiration, and changes in atmospheric boundary layer height [38,39]. Additionally, the high CO_2 and CH_4 mole fractions in the evening and early morning were consistent with the urban vehicle emissions in the rush hours [40]. For CO_2 (Figure 4a), the highest mole fraction was 434.46 ± 1.08 ppm observed at 7:00 (LT) in spring, while the lowest mole fraction was 406.05 ± 0.88 ppm observed at 16:00 (LT) in summer, with the amplitude of 28.41 ± 1.40 ppm. For CH_4 (Figure 4e), both the highest and lowest mole fractions were observed in summer, 2073.8 ± 8.8 ppb at 7:00 (LT) and 2008.9 ± 8.6 ppb at 15:00 (LT), with an amplitude of 64.9 ± 12.3 ppb. The smallest amplitudes were observed in winter, with values of 6.40 ± 1.52 ppm for CO_2 and 19.8 ± 8.5 ppb for CH_4, respectively.

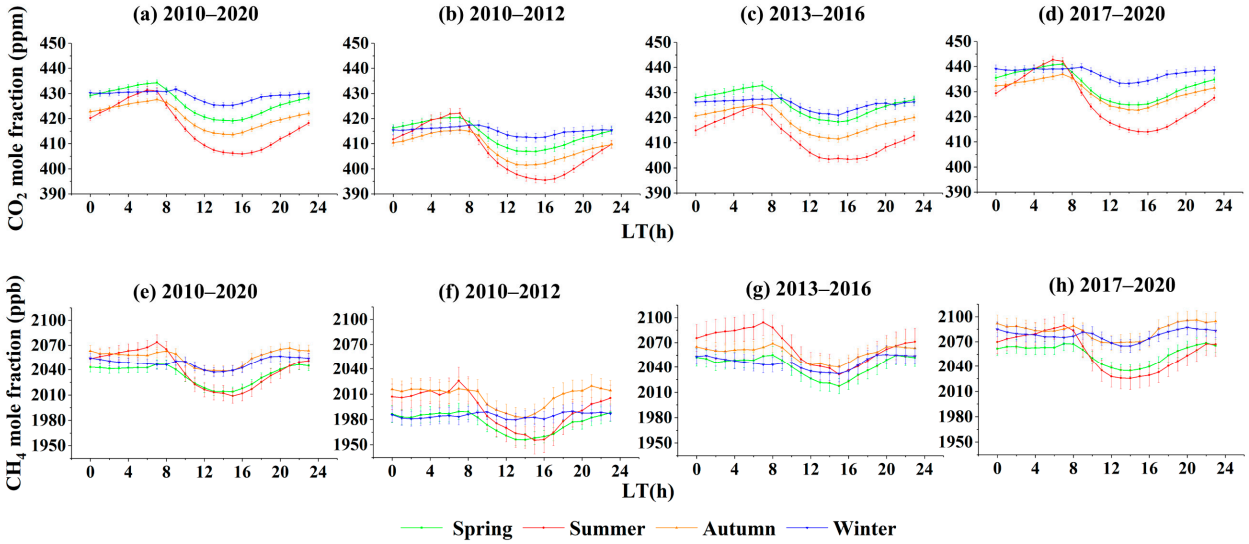

Figure 4. Diurnal CO_2 and CH_4 cycles from 2010 to 2020 at the LAN station. The top and bottom panels show the diurnal cycles of CO_2 (**a**–**d**) and CH_4 (**e**–**h**) in different periods, i.e., 2010–2020 (**a**,**e**), 2010–2012 (**b**,**f**), 2013–2016 (**c**,**g**), 2017–2020 (**d**,**h**), respectively. Different colored lines represent different seasons. The error bars represent 95% confidence intervals.

The diurnal cycle patterns of CO_2 and CH_4 also differ in different periods as shown in Figure 4. From 2013 to 2016, the CO_2 mole fractions in summer mornings were lower than those of other seasons, because the wind speed in this period was lower than that in other seasons, resulting in uneven atmospheric mixing. However, the CH_4 mole fractions in summer were higher than those in the other seasons during the same period, because high temperatures and heavy precipitation were conducive to CH_4 production in wetlands [41,42], especially in 2016, when the precipitation in YRD in summer was 20% to 1 time more than that in previous years. Additionally, the marine seeps from the East China Sea may contribute to the higher CH_4 mole fractions due to the high sea surface temperature during 2013–2016 [9,43]. The peak-to-valley amplitudes of diurnal variation also had significant differences. For CO_2 (Figure 4b–d), the peak-to-valley amplitudes increased with time. For example, the amplitudes for spring, in 2010–2012, 2013–2016, and 2017–2020 were 13.40 ± 2.20 ppm, 14.40 ± 2.22 ppm, and 16.14 ± 1.82 ppm, respectively, which indicated that the LAN station was increasingly affected by anthropogenic activities. However, for CH_4 (Figure 4f–h), the peak-to-valley amplitudes changed with time in different seasons. The amplitude was almost constant in spring. However, in summer, autumn, and winter, the amplitudes were quite different from 2010–2012 and 2013–2020

(about 10 ppb). Although the paddy rice field area decreased in recent decades with the continuous expansion of urbanization area in the YRD region, the rice yields increased, leading to the increase of anthropogenic CH_4 emissions in summer and autumn [42,44]. In addition, energy consumption generally increased in winter, especially of natural gas, leading to higher CH_4 mole fractions [45].

3.3. Variations of Wind-Rose Distribution Pattern

In order to further study the influence of local sources/sinks on the temporal distribution of atmospheric CO_2 and CH_4, the hourly CO_2 and CH_4 mole fractions were clustered by considering the surface wind direction (16 wind directions). The observed mole fractions were divided into March to May as spring, June to August as summer, September to November as autumn, and December to February as winter, to draw the wind rose distribution chart. As shown in Figure 5a,e, there were seasonal differences in CO_2 and CH_4 mole fraction in each wind direction. In spring and winter, the high CO_2 mole fractions mainly came from the NE-ENE-E-ESE-SE sectors in the east, indicating that the high CO_2 mole fractions in spring and summer were mainly caused by the emission transports from the eastern cities of Shanghai, Hangzhou, Suzhou, etc. [23,46,47]. However, the high CO_2 mole fractions came from W-WNW-NNW and SSW-WSW-WSW-W in the west in summer and autumn, respectively, affected by crop straw burning during the harvest [48,49]. Unlike CO_2, the high CH_4 mole fractions in all seasons came from the east, and there were also strong sources in WSW-W-WNW in autumn and winter, possibly due to the combined effect of wetland and urban emissions.

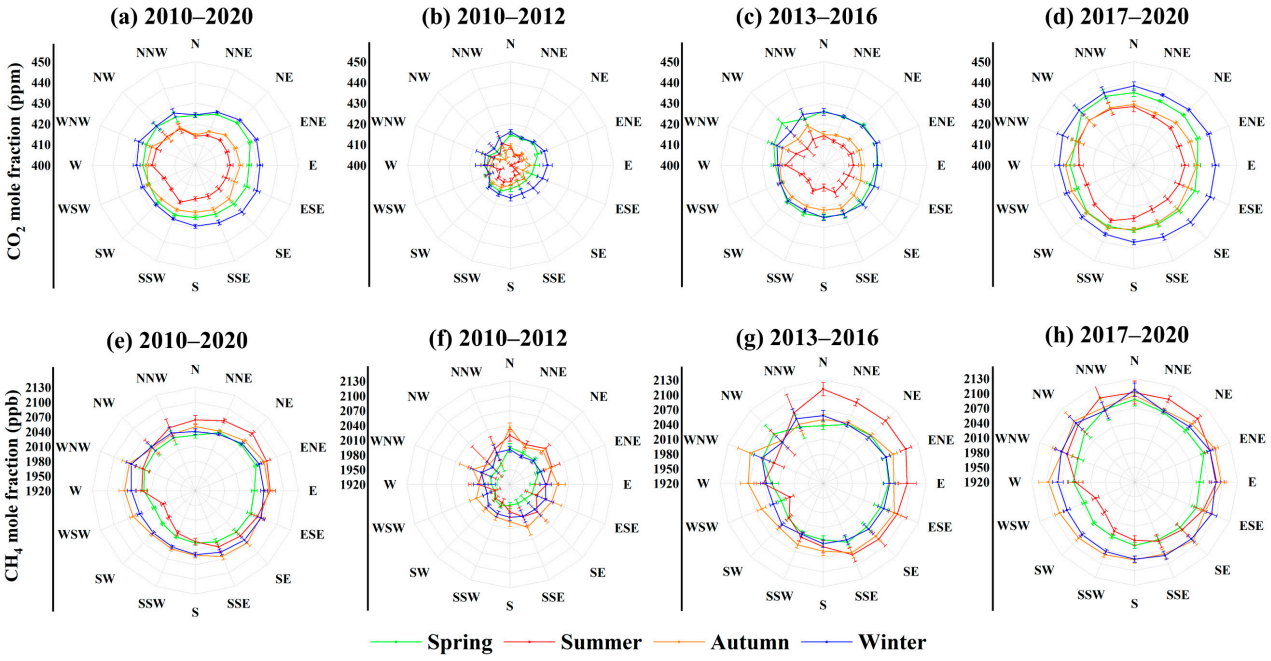

Figure 5. The wind rose distributions of average CO_2 and CH_4 mole fractions in the 16 sectors from 2010 to 2020 at the LAN station. The top and bottom panels show the wind rose distributions of CO_2 (**a**–**d**) and CH_4 (**e**–**h**) in different periods, i.e., 2010–2020 (**a**,**e**), 2010–2012 (**b**,**f**), 2013–2016 (**c**,**g**), 2017–2020 (**d**,**h**), respectively. The different colors represent the CO_2 and CH_4 data for different seasons. The error bars represent 95% confidence intervals.

The wind rose distribution of CO_2 and CH_4 mole fractions showed that the elevated CO_2 and CH_4 mole fractions varied in different periods. During 2010–2012 (Figure 5b,f) and 2013–2016 (Figure 5c,g), there was an obvious increase of CO_2 and CH_4 mole fractions in some wind directions, while during 2017–2020 (Figure 5d,h), the elevated CO_2 and CH_4 mole fractions in all wind directions tended to be uniform, suggesting that CO_2 and CH_4 sources may be present in all wind directions in recent years, which corresponded to the

economy development and increased energy consumption in the YRD region. According to the statistical book of China, the annual Gross Domestic Product (GDP) growth rates of the YRD region have been above 7% except for 2020 [50]. In addition, the magnitude of the enhancement was also increasing with the years. Local surface winds from urban areas had an increasing influence on the atmospheric CO_2 and CH_4 at the LAN station [51,52]. The high CO_2 and CH_4 mole fractions came from different wind directions in different periods, which indicated that sources located upwind were also changing with time. Compared with 2010–2012 and 2013–2016, the elevated CO_2 and CH_4 mole fractions in different wind directions showed a westward shifting trend, while in 2017–2020, the degree of trend weakened and even moved east again. For example, in spring, the high CO_2 and CH_4 mole fractions came from N-NNE-NE-ENE during 2010–2012, WNW-NW during 2013–2016, and NW-NNW-N during 2017–2020. This was mainly due to the industrial development of Anhui Province in the west. In China's 12th Five-Year Plan (2011–2015), the Wanjiang city belt in Anhui Province accepted most of the industrial transfer from the YRD. The number of industrial enterprises increased from 12,432 in 2011 to 19,838 in 2016 but then began to decrease, and the number returned to 17,761 in 2019 [50]. Although the CO_2 and CH_4 mole fractions were dominated by emissions from the core region of YRD in the east of LAN station, the influence of Anhui Province and other central China regions in the west of LAN station could not be neglected.

3.4. Long-Range Transport and Potential Source Distributions

To investigate the contribution of long-range transport, we used the Hybrid Single-Particle Lagrangian Integrated Trajectory (HYSPLIT) to calculate a 72 h back trajectory consistent with the time of the observed regional CO_2 and CH_4 events. We used the back trajectories in January, April, July, and October, respectively, to represent winter, spring, summer, and autumn. Figure 6 and Table 1 showed the results of back trajectory cluster analysis for the four seasons from 2010 to 2020, as well as the average CO_2 and CH_4 mole fractions on each cluster.

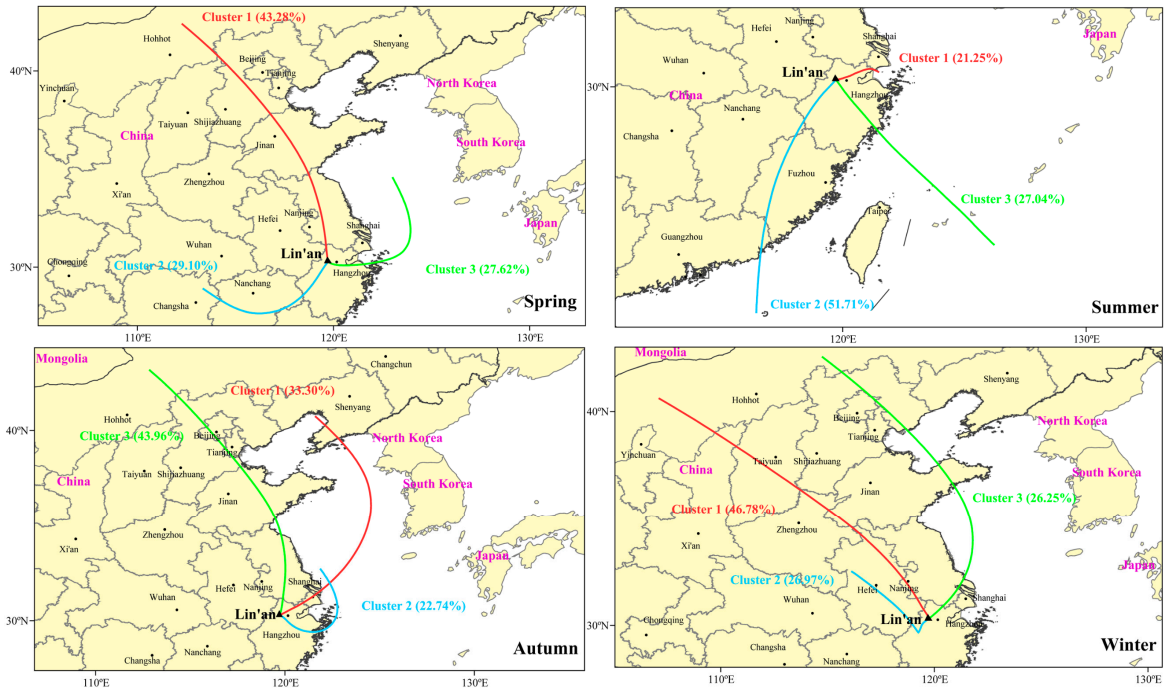

Figure 6. Cluster analysis of 72 h back trajectories at LAN. The black dots represent big cities. The colored lines present different clusters.

Table 1. The statistics of the cluster analysis result for hourly CO_2 and CH_4 data from 2010 to 2020 at the LAN station.

Season	Cluster	Number of Trajectories	Average CO_2 Mole Fraction (ppm)	Average CH_4 Mole Fraction (ppb)
Spring	1	3427	418.19 ± 1.34	1989.3 ± 6.0
	2	2304	420.24 ± 1.73	1990.3 ± 6.1
	3	2187	421.80 ± 1.60	1992.4 ± 8.8
Summer	1	1668	411.10 ± 1.50	2022.1 ± 22.8
	2	4058	405.20 ± 1.04	1934.9 ± 5.8
	3	2122	408.70 ± 1.44	1928.4 ± 17.0
Autumn	1	2637	414.67 ± 1.02	2007.4 ± 7.7
	2	1801	417.66 ± 1.66	2039.5 ± 12.7
	3	3482	414.39 ± 1.09	2000.5 ± 6.8
Winter	1	3701	424.10 ± 1.23	2033.2 ± 6.5
	2	2134	426.17 ± 2.02	2051.4 ± 11.2
	3	2077	425.48 ± 2.28	2025.8 ± 10.7

In spring, the air mass with the highest average CO_2 and CH_4 mole fractions were from the east and northeast (Cluster 3), from the Yellow Sea and the East China Sea. However, after passing through Hangzhou and other cities, the CO_2 and CH_4 mole fractions increased by 2.10 ppm and 2.1 ppb relative to the seasonal average (Table 1). In summer, due to the influence of the monsoon, the air mass mainly came from the eastern, southwestern, and southeastern regions. The highest CO_2 and CH_4 mole fractions were observed in the eastern sector (Cluster 1), which passed over the Hangzhou Bay area, surrounded by Shanghai, Hangzhou and other megacities. Compared to CO_2, the enhancement of CH_4 mole fraction was 80.7 ppb, much larger than the seasonal average, since there are many wetlands (1221.5 km^2 in 2017) in the Hangzhou Bay area in addition to many industries [53]. Thus, both human emission and wetland emission led to high CH_4 mole fractions [23,54]. In autumn, most air masses were from north and northeast China, but the high CO_2 and CH_4 mole fractions came from the Yangtze Estuary and Hangzhou Bay regions, the center of the YRD region. In winter, the air mass mainly came from North China, but the air mass from the northwest region of YRD (Cluster 2) brought the highest CO_2 and CH_4 mole fractions, indicating that the inland region of YRD was becoming strong sources contributed to the LAN station in winter. In conclusion, it is dominant that the YRD region has a great influence on the elevated CO_2 and CH_4 mole fractions at LAN station.

Figures 7 and 8 showed the spatial distribution of CO_2 and CH_4 sources probabilities during the observation period by using the Weighted Potential Source Contribution Function (WPSCF), and the potential sources in different periods were analyzed, namely, 2010–2012, 2013–2016, and 2017–2020. In general, the strongest source was located to the east of the LAN station. The high value of WPSCF was mainly distributed in northern Zhejiang Province, southern Jiangsu Province, and Shanghai. However, due to the impact of industrial transfer, the high value of WPSCF in winter in 2013–2016 (Figures 7k and 8k) was distributed in Anhui Province. High temperature in summer led to more CH_4 emissions from anaerobic activities, and high WPSCF values were distributed in rice fields to the west of LAN Station (Figure 8e) and in Hangzhou Bay area to the east (Figure 8f) [54,55]. In addition, the source areas varied seasonally. The potential source area in summer was mainly located in the south while in spring, autumn, and winter, it was mainly located in the north, due to the difference of the east Asian monsoon.

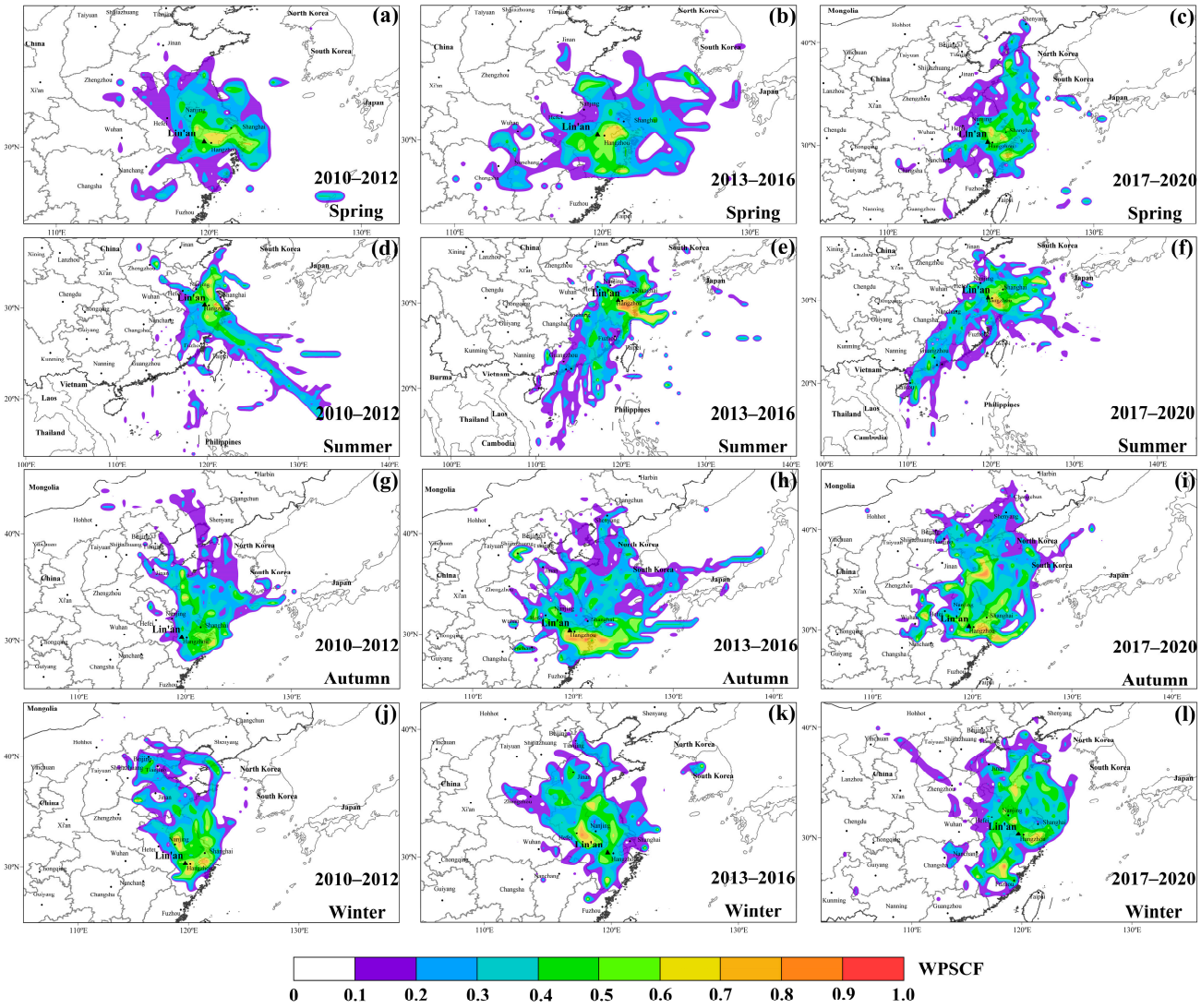

Figure 7. The geographical distribution of CO_2 weighted potential sources in different periods from 2010 to 2020 at the LAN station. The gradient colors represent the intensity of potential source regions in different seasons, i.e., spring (**a**–**c**), summer (**d**–**f**), autumn (**g**–**i**), and winter (**j**–**l**) and different periods, i.e., 2010–2012 (**a**,**d**,**g**,**j**), 2013–2016 (**b**,**e**,**h**,**k**), and 2017–2020 (**c**,**f**,**i**,**l**).

The potential source areas of CO_2 and CH_4 varied over the periods, almost always increasing with time, and emission intensity from the core area has also been strengthened. For example, in the spring during 2010–2012 (Figure 7a), CO_2 sources were mainly concentrated in the YRD region. However, during 2013–2016 (Figure 7b), CO_2 sources shifted from the western area to inland China. As a result, it can be concluded that the atmospheric CO_2 and CH_4 at LAN were more severely influenced by regional sources and sinks, due to the rapid economic development in the YRD region. The expansion pattern of strong sources suggested that inland provinces surrounding the YRD, such as Anhui Province, were becoming stronger CO_2 and CH_4 emitters, in addition to the eastern coastal region of the YRD where LAN was located [56]. In recent years, as a member of the YRD region, Anhui Province has been developing rapidly, with the number of factories (12,432 in 2011 and increased to 17,761 in 2019 [50]) and gross value of industrial output (2.59 trillion yuan in 2011 and increased to 4.34 trillion yuan in 2016 [50]) increasing, which caused a large amount of CO_2 and CH_4 to transfer eastward to Zhejiang Province, Shanghai and Jiangsu Province [57].

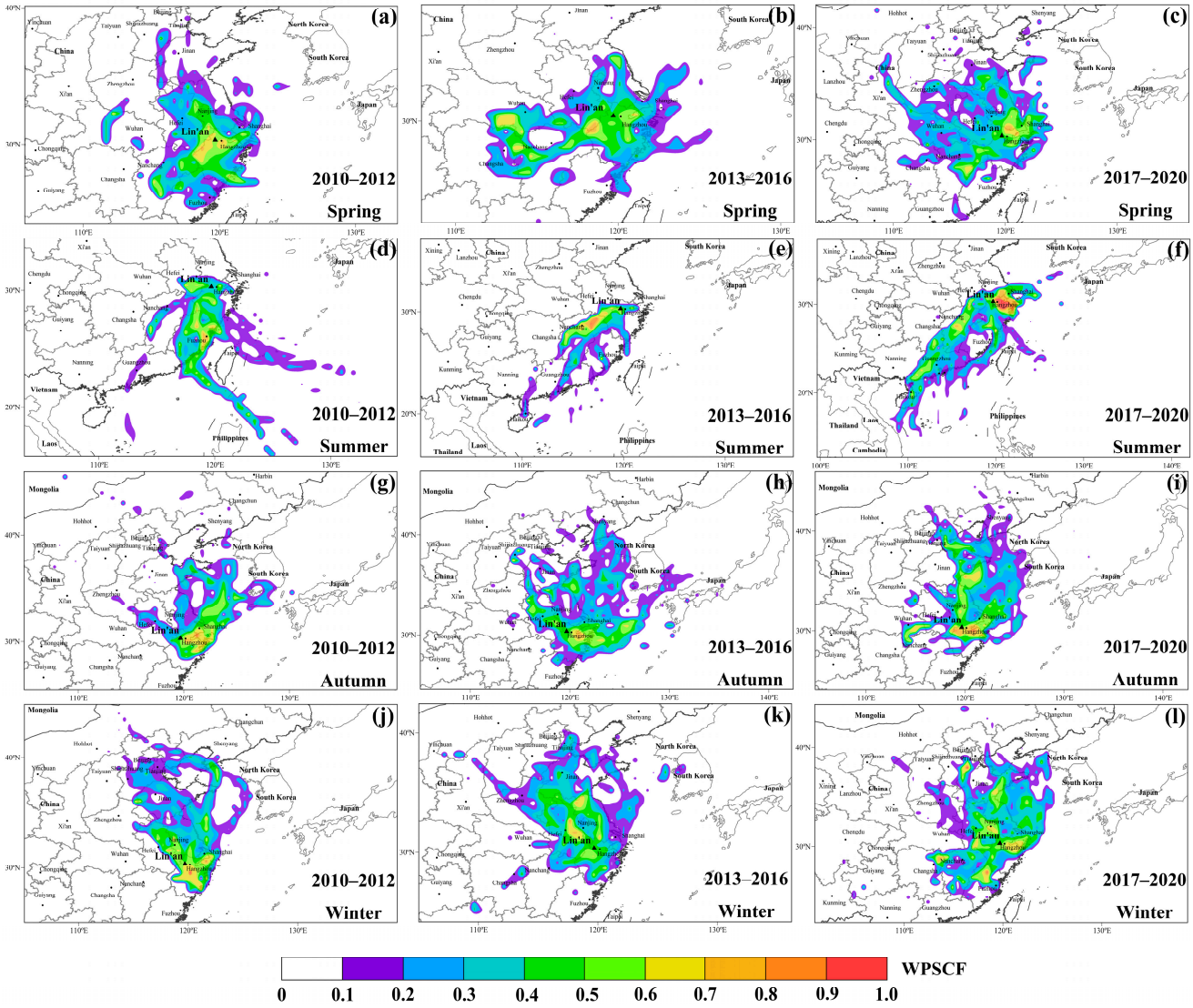

Figure 8. The geographical distribution of CH_4 weighted potential sources in different periods from 2010 to 2020 at the LAN station. The gradient colors represent the intensity of potential source regions in different seasons, i.e., spring (**a**–**c**), summer (**d**–**f**), autumn (**g**–**i**), and winter (**j**–**l**) and different periods, i.e., 2010–2012 (**a**,**d**,**g**,**j**), 2013–2016 (**b**,**e**,**h**,**k**), and 2017–2020 (**c**,**f**,**i**,**l**).

3.5. Variation of Long-Term Records

3.5.1. Seasonal Cycles

Figure 9 shows the monthly changes in regional CO_2 and CH_4 mole fractions in various periods from 2010 to 2020. On the whole, the monthly variation trend of regionally representative CO_2 and CH_4 mole fractions at the LAN region was almost identical in each period. The CO_2 mole fractions were high in winter and low in summer, while the CH_4 mole fractions fluctuated and were low in April and July. The monthly variation trend of CO_2 mole fractions was similar to the observations at the SDZ station and LFS station in China [21,58]. However, there was also an obvious difference for CH_4, which was mainly caused by the seasonal variations of vegetation growth and energy consumption in each region [45]. The CH_4 mole fractions at LFS peaked in summer and autumn due to the emissions from rice fields [21]. The seasonal variation of CH_4 from south and northwest at SDZ showed double peak and single peak, with the lowest in May and July, respectively [20], while the seasonal variation of CH_4 at LAN showed triple peaks, with the lowest in July. Compared with the other periods, CO_2 and CH_4 mole fractions from 2010 to 2012 peaked in February. Local customs such as setting off fireworks and

worshiping during the Chinese Spring Festival in February contributed to massive CO_2 and CH_4 emissions [58], but megacities in the YRD such as Hangzhou, Nanjing, and Shanghai have adopted strict bans on fireworks since 2014, leading to a reduction in emissions. The monthly peak and valley amplitudes of CO_2 and CH_4 mole fractions also changed over time. For CO_2, peak-to-valley amplitudes were 19.49 ± 0.90 ppm from 2010 to 2012, increased to 23.06 ± 1.24 ppm from 2013 to 2016, and 23.47 ± 1.13 ppm from 2017 to 2020. The same is true for CH_4, which revealed that the LAN was intensively affected by stronger regional sources over time.

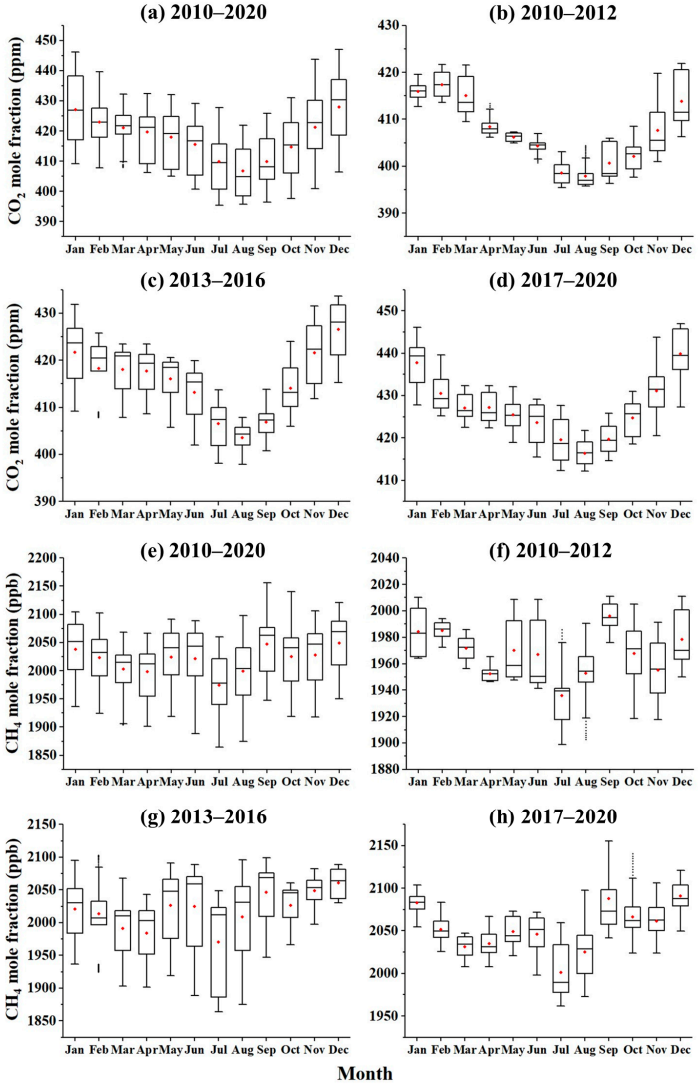

Figure 9. Monthly variations in regional CO_2 and CH_4 mole fractions from 2010 to 2020 at LAN. The top and bottom panels show the monthly variations of CO_2 (**a**–**d**) and CH_4 (**e**–**h**) in different periods, i.e., 2010–2020 (**a**,**e**), 2010–2012 (**b**,**f**), 2013–2016 (**c**,**g**), 2017–2020 (**d**,**h**), respectively. The top and bottom edges of the box describe the 25th, median, and 75th percentiles from bottom to top. The bottom and the top reach the minimum and 1.5 times interquartile range (IQR). The black dots represent outliers. The red dots represent averages.

Figure 10 displayed the average monthly variation of regional and local mole fractions at LAN and the simulated surface values from the Marine Boundary Layer (MBL) reference calculated by the National Oceanic & Atmospheric Administration/Global Monitoring Laboratory (NOAA/GML) from 2010–2020 (https://gml.noaa.gov/ccgg/mbl/mbl.html, accessed on 31 May 2022), also compared with the results at Mt. Waliguan (WLG; 36.28° N, 100.09° E, 3816 m a.s.l.; 2010–2019) [59]. On the whole, the monthly regional CO_2 and

CH_4 mole fractions varied greatly at the LAN station. The CO_2 mole fractions were mainly low in summer and high in winter, with a peak-to-valley amplitude of 21.22 ± 1.54 ppm. In contrast, the CH_4 mole fractions were consistently low in summer and high in spring and autumn, with a peak-to-valley amplitude of 75.1 ± 7.8 ppb. The CO_2 and CH_4 mole fractions at the LAN station were higher than the MBL values and the results at WLG. It was clear that atmospheric CO_2 and CH_4 mole fractions were influenced by regional terrestrial ecosystems as well as anthropogenic emissions [60,61]. The monthly variation of average CO_2 mole fractions at LAN was unimodal, with the lowest in August and the highest in December. Cooler temperatures in winter led to increasing energy consumption and consequently higher CO_2 and CH_4 mole fractions [22,62]. On the contrary, in summer, the CO_2 mole fractions decreased due to the intense plant photosynthesis and the higher atmospheric boundary layer height [36]. Due to the heavy photochemical pollution in the YRD in July, the concentrations of ·OH in the atmosphere were high, and strengthened the CH_4 sinks [38]. At the same time, because the LAN station was in the subtropical monsoon area, the CH_4 mole fractions were mainly affected by marine air mass in summer. Although the ocean was a significant source of atmospheric CH_4, its emission was much lower than that of the YRD urban agglomeration, so the CH_4 mole fractions tended to be low by the dilution effect of marine air mass [37,43]. In September, when the solar radiation is weak, the concentrations of ·OH in the atmosphere decreased and the sinks of CH_4 weakened [38].

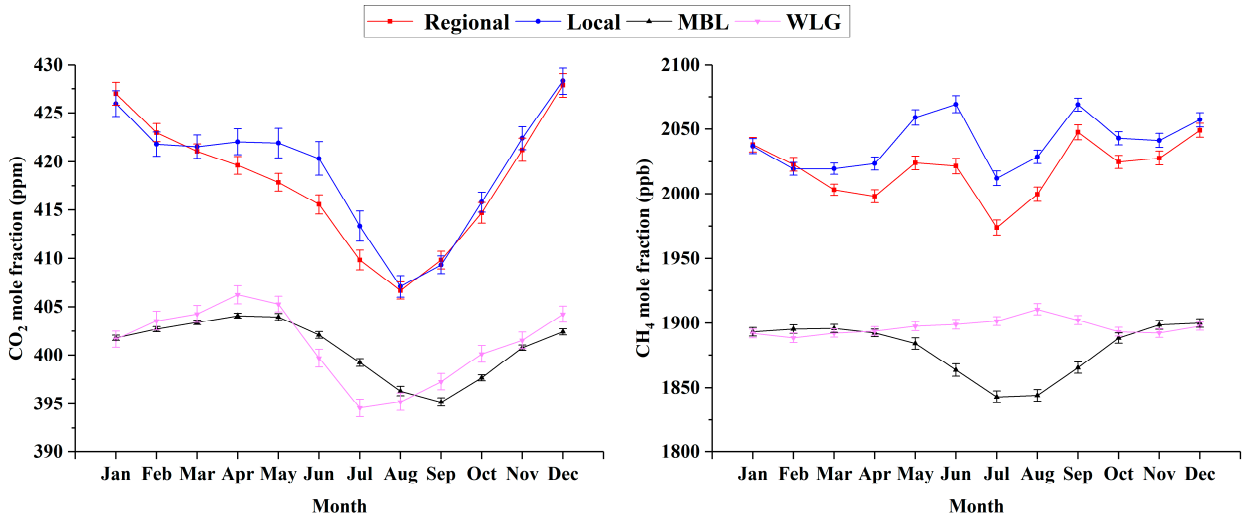

Figure 10. Seasonal variations of regional and local CO_2 and CH_4 mole fractions at LAN (2010–2020). Compared also with the results at Mt. Waliguan (WLG; 2010–2019) and Marine Boundary Layer reference (MBL; 2010–2019) surface values (30° N) computed from NOAA/ESRL. Error bars indicate standard deviations with confidence intervals of 95%.

3.5.2. Long-Term Trends

The growth rates of CO_2 and CH_4 from 2010 to 2020 calculated by using the first derivative of the trend curve were presented in Figure 11. The regional average annual growth rates of CO_2 and CH_4 at LAN were 2.57 ± 0.14 ppm yr^{-1} and 10.3 ± 1.3 ppb yr^{-1}. Compared with previous studies (3.7 ± 1.2 ppm yr^{-1} for CO_2 and 8.0 ± 1.2 ppb yr^{-1} for CH_4 in 2009–2010) at LAN station, the growth rates of CO_2 were lower, while the growth rates of CH_4 were higher [30,63]. Moreover, as the Chinese government announced a carbon reduction strategy to reduce CO_2 emissions, the intense emissions from heavy industries were restricted in recent years [19]. From 2010 to 2015, the annual increment of carbon emissions in the Yangtze River Delta region was about 40.3 Mt CO_2 yr^{-1} but decreased to 24.6 Mt CO_2 yr^{-1} in recent years (2016–2019) [64].

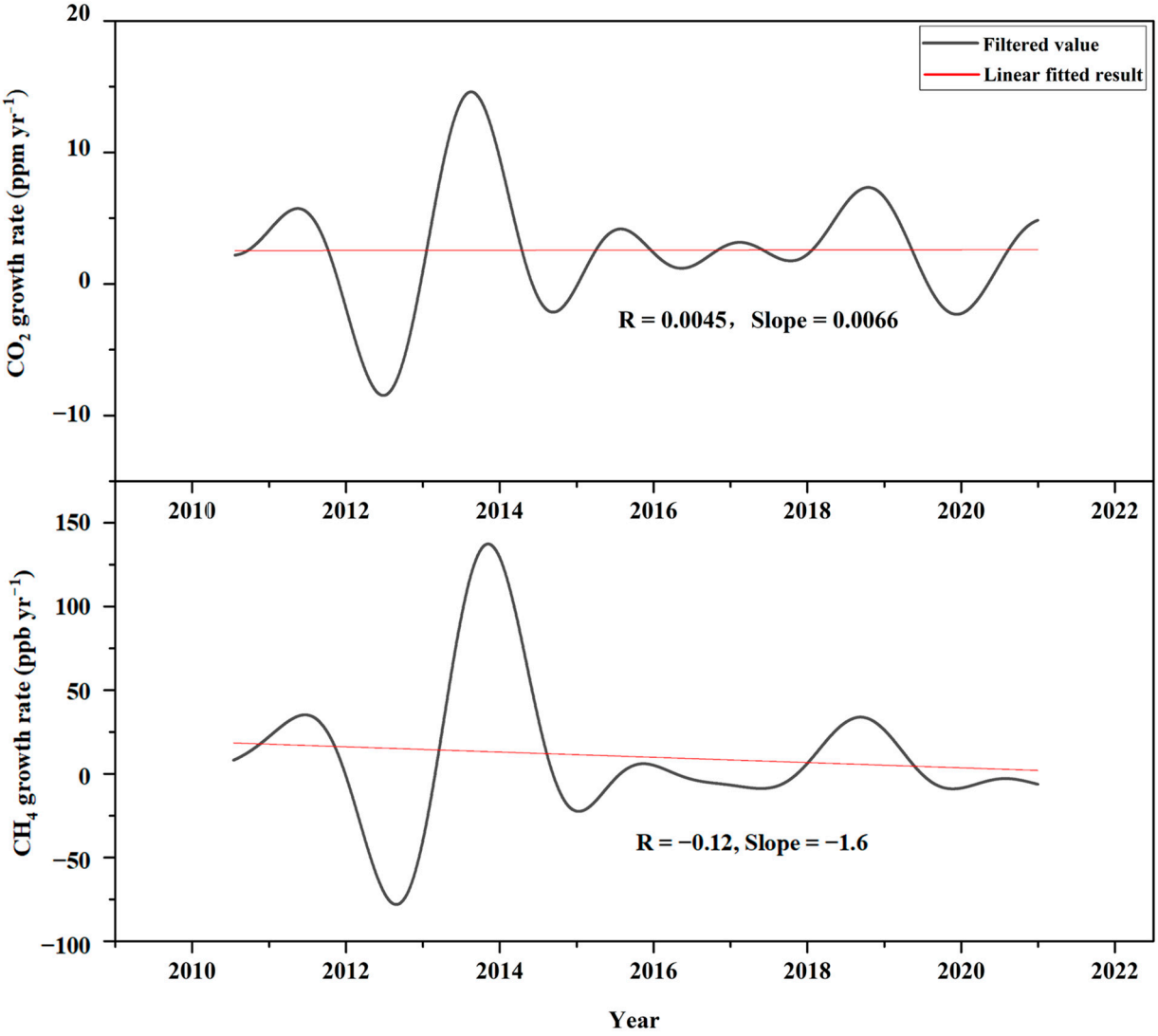

Figure 11. The annual growth rates of the atmospheric CO_2 and CH_4 from 2010 to 2020 at the LAN station. The black line represents the filtered value, which was calculated from the first derivative of the trend curves. The red line represents the slope, which was calculated by linear regression.

The annual growth rates of CO_2 and CH_4 were both higher than the global average (2.40 ppm yr^{-1} for CO_2 and 8.0 ppb yr^{-1} for CH_4) over the past decade [2,65]. As shown in Table 2, the observed results of CO_2 and CH_4 at LAN were higher than those at the background site in China. The observations from Lamto in West Africa from 2008 to 2018 showed that the annual growth rates of CO_2 and CH_4 were approximately 2.24 ppm yr^{-1} and 7 ppb yr^{-1}, respectively, both lower than those at LAN [66]. Nguyen et al. [67] presented 20-year (2001–2020) records of atmospheric CO_2 at Lutjewad in the Netherlands and Mace Head in Ireland, with annual growth rates of 2.31 ± 0.07 ppm yr^{-1} and 2.22 ± 0.04 ppm yr^{-1}, respectively. The higher growth rate indicated that there was a strong difference between economically developed zones and remote areas, and the LAN station was strongly influenced by regional sources/sinks [59,68]. In addition, the annual average growth rate of CO_2 at LAN was lower than that at LFS and SDZ because LFS and SDZ were located in Northeast and North China, respectively, where fossil fuel consumption was high in heavy industry and winter heating [21,58]. However, the annual growth rate of CH_4 was completely opposite, which was mainly due to high emissions from rice fields and wetland in the YRD [42].

Table 2. Comparison of annual average CO_2 and CH_4 growth rates at the background stations of Lin'an (LAN), Longfengshan (LFS), Shangdianzi (SDZ), Mt. Waliguan (WLG) in China.

Site	Years	CO_2 Growth Rate (ppm yr^{-1})	CH_4 Growth Rate (ppb yr^{-1})	Ref.
LAN, China	2010–2013	3.00 ± 0.38	16.1 ± 3.3	This study
	2010–2016	2.52 ± 0.21	13.8 ± 2.0	
	2010–2020	2.57 ± 0.14	10.3 ± 1.3	
LFS, China	2009–2013	3.10 ± 0.02	8.0 ± 0.04	Fang et al. [21]
SDZ, China	2009–2013	3.80 ± 0.01	10.0 ± 0.1	Fang et al. [20]
WLG, China	2010–2016	2.45 ± 0.02	8.2 ± 0.1	Guo et al. [68]

The growth rate of CO_2 and CH_4 at the LAN fluctuated greatly in the early stage, decreased rapidly in 2012 and 2014, leveled off again in 2016–2018, and then fluctuated slightly after 2018, which may be caused by the Nanjing Youth Olympic Games in 2014, the Hangzhou G20 Summit in 2016, and the COVID-19 event in early 2020 [69,70]. During the Nanjing Youth Olympic Games in 2014 and the Hangzhou G20 Summit in 2016, the Chinese government implemented a series of joint anti-pollution measures, such as traffic restrictions and factory shutdowns, in cities in the YRD region [25]. Xu et al. [71] found that during the Nanjing Youth Olympic Games, the YRD region has actually reduced coal emissions by 5%, and the atmospheric CO_2 mole fractions were lower than at other times. The carbon emissions of Jiangsu Province decreased by 38% during the period, mainly in the power industry, non-metallic mineral production, and manufacturing combustion [72]. Similarly, Pu et al. [73] found that CO_2 mole fractions in urban and exurbs of Hangzhou have decreased significantly compared to the same period in 2015, due to the impact of the Hangzhou G20 Summit. In addition, the COVID-19 pandemic has significantly reduced China's carbon emissions in February–March 2020, but the variation of growth rate was slight due to the huge atmospheric storage and long lifetime [74]. The COVID-19 pandemic lockdown lasted nearly a month, and CO_2 emissions rebounded as city lockdowns were lifted and production resumed [75]. Therefore, short-term emission reduction activities cannot effectively inhibit the rising trend of CO_2 mole fraction.

The growth rate of regional CO_2 was almost stable and positive in the long term, except in 2012, resulting in a continuous rise of the regional CO_2 mole fractions, which indicated that although a series of management steps to limit CO_2 emissions have been taken in the YRD region (e.g., vehicle electrification, industrial restructuring, and carbon trading), there was still a long way to achieve the carbon neutrality goal [31,76–78]. The high growth rate of CH_4 in the early period may be attributed to the increase in natural gas consumption. As a clean energy source, natural gas is gradually replacing coal, oil, and other traditional energy sources, for example, with the coal-to-gas policy in China [79]. Moreover, China's West-to-East Power Transmission Project has made it convenient for YRD to obtain natural gas. The number of natural-gas-fueled vehicles in China has increased fast, with about 6000 in 2000 increasing to 6.08 million in 2017. Especially in 2012–2014, the annual growth rate of natural-gas-fueled vehicles reached about 1.00 million per year [80]. Taking Zhejiang Province as an example, the proportion of natural gas in total energy consumption increased rapidly during 2013–2014 (3.6%–4.9%) and 2017–2018 (6.0%–7.5%) but decreased in 2020 (7.4%), which was basically consistent with the CH_4 growth rate [50]. China implemented the Air Pollution Prevention and Control Action Plan in September 2013, which resulted in a significant decrease in the growth rate of CO_2 and CH_4. With the implementation of anthropogenic pollution control measures in the YRD (e.g., electric vehicles promotion and energy structure optimization), the regional CH_4 growth rate has been declining in the long run [81,82]. Finally, due to the absence of CO_2 data from October 2012 to June 2013 and CH_4 data from October 2012 to October 2013, there may be bias on the estimation on the CO_2 and CH_4 growth rates.

4. Conclusions

In this study, we present an 11-year (from 2010 to 2020) ground-based observation of atmospheric CO_2 and CH_4 at the Lin'an (LAN) regional background station and analyze the changing characters of those gases to understand the influence of anthropogenic emissions. Our results show that with the development of the Chinese economy, the observed CO_2 and CH_4 mole fractions in recent years were severely influenced by local sources, and only 16.31% of CO_2 and 14.34% of CH_4 mole fractions represent the events on the regional scale. The regional background mole fractions of CO_2 and CH_4 in the YRD region had distinct diurnal distribution and seasonal fluctuation characteristics. The local surface wind impacts, long-range transport, and potential source distributions in different periods all indicated that the LAN station was mainly affected by the source and sink in the YRD region, and Anhui Province in the west of YRD has been becoming a strong contributor to CO_2 and CH_4 emissions. In the long run, the growth rates of CH_4 at the LAN station were continuously decreasing, and the growth rates of CO_2 remained stable, due to the strict emission control measures in the YRD region. However, with the rapid growth of the regional economy, CO_2 and CH_4 mole fractions were still increasing with the years except for some specific years. We found that LAN was increasingly influenced by local anthropogenic activities. In addition, the complex changes and high average annual growth rates of CO_2 and CH_4 indicated that controlling CO_2 and CH_4 emissions remained a priority for the Chinese government.

Author Contributions: Conceptualization, S.L. and S.F.; methodology, K.J., S.L. and S.F.; validation, Q.M. and S.F.; formal analysis, K.J.; writing—original draft preparation, K.J.; resources, Q.M. and S.F.; writing—review and editing, K.J., K.Z., Y.L., Y.C., S.Q., X.Q., H.X., H.H., J.L. and S.F.; funding acquisition, S.F. All authors have read and agreed to the published version of the manuscript.

Funding: This research was funded by the National Key Research and Development Program of China grant number (2020YFA0607502).

Institutional Review Board Statement: Not applicable.

Informed Consent Statement: Not applicable.

Data Availability Statement: All CO_2, CH_4, and meteorological data were attained by the National Reference Climatological Station; data for backward trajectory and potential source analysis were from Global Data Assimilation System, ftp://arlftp.arlhp.noaa.gov/pub/archives/gdas1/ accessed on 31 May 2023.

Acknowledgments: This work was supported by the National Key Research and Development Program of China (2020YFA0607502). We also thank the staff who have contributed to the system installation and maintenance at the Lin'an station in past years.

Conflicts of Interest: The authors declare no conflict of interest.

References

1. Jain, A.K.; Briegleb, B.P.; Minschwaner, K.; Wuebbles, D.J. Radiative forcings and global warming potentials of 39 greenhouse gases. *J. Geophys. Res.* **2000**, *105*, 20773–20790. [CrossRef]
2. WMO Greenhouse Gas Bulletin: The State of Greenhouse Gases in the Atmosphere Based on Global Observations through 2021. 2022. Available online: https://community.wmo.int/en/activity-areas/gaw (accessed on 21 March 2023).
3. IPCC. *Climate Change 2014: Synthesis Report*; Contribution of Working Groups I, II and III to the Fifth Assessment Report of the Intergovernmental Panel on Climate Change; Core Writing Team, Pachauri, R.K., Meyer, L.A., Eds.; IPCC: Geneva, Switzerland, 2014; 151p.
4. Artuso, F.; Chamard, P.; Piacentino, S.; Sferlazzo, D.M.; De Silvestri, L.; di Sarra, A.; Meloni, D.; Monteleone, F. Influence of transport and trends in atmospheric CO_2 at Lampedusa. *Atmos. Environ.* **2009**, *43*, 3044–3051. [CrossRef]
5. Sabine, C.L.; Feely, R.A.; Gruber, N.; Key, R.M.; Lee, K.; Bullister, J.L.; Wanninkhof, R.; Wong, C.S.; Wallace, D.W.; Tilbrook, B.; et al. The oceanic sink for anthropogenic CO_2. *Science* **2004**, *305*, 367–371. [CrossRef]
6. Pan, Y.; Birdsey, R.A.; Fang, J.; Houghton, R.; Kauppi, P.E.; Kurz, W.A.; Phillips, O.L.; Shvidenko, A.; Lewis, S.L.; Canadell, J.G.; et al. A large and persistent carbon sink in the world's forests. *Science* **2011**, *333*, 988–993. [CrossRef]
7. Ballantyne, A.P.; Alden, C.B.; Miller, J.B.; Tans, P.P.; White, J.W. Increase in observed net carbon dioxide uptake by land and oceans during the past 50 years. *Nature* **2012**, *488*, 70–72. [CrossRef]

8. Peters, W.; Jacobson, A.R.; Sweeney, C.; Andrews, A.E.; Conway, T.J.; Masarie, K.; Miller, J.B.; Bruhwiler, L.M.; Petron, G.; Hirsch, A.I.; et al. An atmospheric perspective on North American carbon dioxide exchange: CarbonTracker. *Proc. Natl. Acad. Sci. USA* **2007**, *104*, 18925–18930. [CrossRef] [PubMed]
9. Archer, D.; Buffett, B.; Brovkin, V. Ocean methane hydrates as a slow tipping point in the global carbon cycle. *Proc. Natl. Acad. Sci. USA* **2009**, *106*, 20596–20601. Available online: https://www.pnas.org/cgi/doi/10.1073/pnas.0800885105 (accessed on 30 June 2022). [CrossRef] [PubMed]
10. Dlugokencky, E.J.; Nisbet, E.G.; Fisher, R.; Lowry, D. Global atmospheric methane: Budget, changes and dangers, Philos. Trans. A Math. *Phys. Eng. Sci.* **2011**, *369*, 2058–2072. [CrossRef]
11. Chang, J.; Peng, S.; Ciais, P.; Saunois, M.; Dangal, S.R.S.; Herrero, M.; Havlik, P.; Tian, H.; Bousquet, P. Revisiting enteric methane emissions from domestic ruminants and their $\delta^{13}C_{CH4}$ source signature. *Nat. Commun.* **2019**, *10*, 3420. [CrossRef] [PubMed]
12. Fujita, R.; Morimoto, S.; Maksyutov, S.; Kim, H.S.; Arshinov, M.; Brailsford, G.; Aoki, S.; Nakazawa, T. Global and regional CH_4 emissions for 1995–2013 derived from atmospheric CH_4, δ^{13}C-CH_4, and δD-CH_4 observations and a chemical transport model. *J. Geophys. Res.* **2020**, *125*, e2020JD032903. [CrossRef]
13. Bousquet, P.; Ciais, P.; Miller, J.B.; Dlugokencky, E.J.; Hauglustaine, D.A.; Prigent, C.; Van der Werf, G.R.; Peylin, P.; Brunke, E.G.; Carouge, C.; et al. Contribution of anthropogenic and natural sources to atmospheric methane variability. *Nature* **2006**, *443*, 439–443. [CrossRef] [PubMed]
14. Dlugokencky, E.J.; Bruhwiler, L.; White, J.W.C.; Emmons, L.K.; Novelli, P.C.; Montzka, S.A.; Masarie, K.A.; Lang, P.M.; Crotwell, A.M.; Miller, J.B.; et al. Observational constraints on recent increases in the atmospheric CH_4 burden. *Geophys. Res. Lett.* **2009**, *36*, L18803. [CrossRef]
15. Kirschke, S.; Bousquet, P.; Ciais, P.; Saunois, M.; Canadell, J.G.; Dlugokencky, E.J.; Bergamaschi, P.; Bergmann, D.; Blake, D.R.; Bruhwiler, L.; et al. Three decades of global methane sources and sinks. *Nat. Geogr.* **2013**, *6*, 813–823. [CrossRef]
16. Bousquet, P.; Ringeval, B.; Pison, I.; Dlugokencky, E.J.; Brunke, E.G.; Carouge, C.; Chevallier, F.; Fortems-Cheiney, A.; Frankenberg, C.; Hauglustaine, D.A.; et al. Source attribution of the changes in atmospheric methane for 2006–2008. *Atmos. Chem. Phys.* **2011**, *11*, 3689–3700. [CrossRef]
17. Zhang, F.; Fukuyama, Y.; Wang, Y.; Fang, S.; Li, P.; Fan, T.; Zhou, L.; Liu, X.; Meinhardt, F.; Emiliani, P. Detection and attribution of regional CO_2 concentration anomalies using surface observations. *Atmos. Environ.* **2015**, *123*, 88–101. [CrossRef]
18. Patra, P.K.; Saeki, T.; Dlugokencky, E.J.; Ishijima, K.; Umezawa, T.; Ito, A.; Aoki, S.; Morimoto, S.; Kort, E.A.; Crotwell, A.; et al. Regional Methane Emission Estimation Based on Observed Atmospheric Concentrations (2002–2012). *J. Meteorol. Soc. Jpn. Ser. II* **2016**, *94*, 91–113. [CrossRef]
19. Liu, S.; Fang, S.; Liu, P.; Liang, M.; Guo, M.; Feng, Z. Measurement report: Changing characteristics of atmospheric CH_4 in the Tibetan Plateau: Records from 1994 to 2019 at the Mount Waliguan station. *Atmos. Chem. Phys.* **2021**, *21*, 393–413. [CrossRef]
20. Fang, S.; Tans, P.; Dong, F.; Zhou, H.; Luan, T. Characteristics of atmospheric CO_2 and CH_4 at the Shangdianzi regional background station in China. *Atmos. Environ.* **2016**, *131*, 1–8. [CrossRef]
21. Fang, S.; Tans, P.; Yao, B.; Luan, T.; Wu, Y.; Yu, D. Study of atmospheric CO_2 and CH_4 at Longfengshan WMO/GAW regional station: The variations, trends, influence of local sources/sinks, and transport. *Sci. China Earth Sci.* **2017**, *60*, 1886–1895. [CrossRef]
22. Gregg, J.S.; Andres, R.J.; Marland, G. China Emissions pattern of the world leader in CO_2 emissions from fossil fuel consumption and cement production. *Geophys. Res. Lett.* **2008**, *35*, L08806. [CrossRef]
23. Chan, C.; Yao, X. Air pollution in mega cities in China. *Atmos. Environ.* **2008**, *42*, 1–42. [CrossRef]
24. Du, M.; Peng, C.; Wang, X.; Chen, H.; Wang, M.; Zhu, Q. Quantification of methane emissions from municipal solid waste landfills in China during the past decade. *Renew. Sustain. Energy Rev.* **2017**, *78*, 272–279. [CrossRef]
25. Chen, Y.; Ma, Q.; Lin, W.; Xu, X.; Yao, J.; Gao, W. Measurement report: Long-term variations in carbon monoxide at a background station in China's Yangtze River Delta region. *Atmos. Chem. Phys.* **2020**, *20*, 15969–15982. [CrossRef]
26. Shan, Y.; Huang, Q.; Guan, D.; Hubacek, K. China CO_2 emission accounts 2016–2017. *Sci. Data* **2020**, *7*, 54. [CrossRef] [PubMed]
27. Fang, S.; Tans, P.; Steinbacher, M.; Zhou, L.; Luan, T. Comparison of the regional CO_2 mole fraction filtering approaches at a WMO/GAW regional station in China. *Atmos. Meas. Tech.* **2015**, *8*, 5301–5313. [CrossRef]
28. Crosson, E.R. A cavity ring-down analyzer for measuring atmospheric levels of methane, carbon dioxide, and water vapor. *Appl. Phys. B* **2008**, *92*, 403–408. [CrossRef]
29. Welp, L.R.; Keeling, R.F.; Weiss, R.F.; Paplawsky, W.; Heckman, S. Design and performance of a Nafion dryer for continuous operation at CO_2 and CH_4 air monitoring sites. *Atmos. Meas. Tech.* **2013**, *6*, 1217–1226. [CrossRef]
30. Fang, S.; Zhou, L.; Masarie, K.; Xu, L.; Rella, C.W. Study of atmospheric CH_4 mole fractions at three WMO/GAW stations in China. *J. Geophys. Res.* **2013**, *118*, 4874–4886. [CrossRef]
31. Liu, S.; Fang, S.; Liang, M.; Sun, W.; Feng, Z. Temporal patterns and source regions of atmospheric carbon monoxide at two background stations in China. *Atmos. Res.* **2019**, *220*, 169–180. [CrossRef]
32. Ashbaugh, L.L.; Malm, W.C.; Sadeh, W.Z. A residence time probability analysis of sulfur concentrations at grand-canyon-national-park. *Atmos. Environ.* **1985**, *19*, 1263–1270. [CrossRef]
33. Polissar, A.V.; Hopke, P.K.; Paatero, P.; Kaufmann, Y.J.; Hall, D.K.; Bodhaine, B.A.; Dutton, E.G.; Harris, J.M. The aerosol at Barrow, Alaska: Long-term trends and source locations. *Atmos. Environ.* **1999**, *33*, 2441–2458. [CrossRef]
34. Thoning, K.W.; Tans, P.P.; Komhyr, W.D. Atmospheric carbon dioxide at Mauna Loa observatory: 2. Analysis of the NOAA GMCC data, 1974–1985. *J. Geophys. Res.* **1989**, *94*, 8549–8565. [CrossRef]

35. Zhao, J.; Zhang, S.; Yang, K.; Zhu, Y.; Ma, Y. Spatio-Temporal Variations of CO_2 Emission from Energy Consumption in the Yangtze River Delta Region of China and Its Relationship with Nighttime Land Surface Temperature. *Sustainability* **2020**, *12*, 8388. [CrossRef]
36. Cheng, Y.; An, X.; Yun, F.; Zhou, L.; Liu, L.; Fang, S.; Xu, L. Simulation of CO_2 variations at Chinese background atmospheric monitoring stations between 2000 and 2009: Applying a CarbonTracker model. *Chin. Sci. Bull.* **2013**, *58*, 3986–3993. [CrossRef]
37. Liu, L.; Tans, P.; Xia, L.; Zhou, L.; Zhang, F. Analysis of patterns in the concentrations of atmospheric greenhouse gases measured in two typical urban clusters in China. *Atmos. Environ.* **2018**, *173*, 343–354. [CrossRef]
38. Rigby, M.; Montzka, S.A.; Prinn, R.G.; White, J.W.C.; Young, D.; O'Doherty, S.; Lunt, M.F.; Ganesan, A.L.; Manning, A.J.; Simmonds, P.G.; et al. Role of atmospheric oxidation in recent methane growth. *Proc. Natl. Acad. Sci. USA* **2017**, *114*, 5373–5377. [CrossRef] [PubMed]
39. Niu, Z.; Zhou, W.; Feng, X.; Hou, Y.; Chen, N.; Du, H.; Wu, S.; Fu, Y.; Lu, X.; Cheng, P.; et al. Determining diurnal fossil fuel CO_2 and biological CO_2 by $\Delta^{14}CO_2$ observation on certain summer and winter days at Chinese background sites. *Sci. Total Environ.* **2020**, *718*, 136864. [CrossRef]
40. Hao, Y.; Song, X. Research on trends and spatial distribution of vehicular emissions and its control measure assessment in the Yangtze River Delta, China, for 1999-2015. *Environ. Sci. Pollut. Res. Int.* **2018**, *25*, 36503–36517. [CrossRef]
41. Wania, R.; Melton, J.; Hodson, E.; Poulter, B.; Ringeval, B.; Spahni, R.; Bohn, T.; Avis, A.; Chen, G.; Eliseev, A.V.; et al. Present state of global wetland extent and wetland methane modelling: Methodology of a model inter-comparison project (WETCHIMP). *Geosci. Model Dev.* **2013**, *6*, 617–641. [CrossRef]
42. Huang, W.; Griffis, T.J.; Hu, C.; Xiao, W.; Lee, X.H. Seasonal Variations of CH_4 Emissions in the Yangtze River Delta Region of China Are Driven by Agricultural Activities. *Adv. Atmos. Sci.* **2021**, *38*, 1537–1551. [CrossRef]
43. Sun, M.; Zhang, G.; Ma, X.; Cao, X.; Mao, X.; Li, J.; Ye, W.; Liu, S. Dissolved methane in the East China Sea: Distribution, seasonal variation and emission. *Mar. Chem.* **2018**, *202*, 12–26. [CrossRef]
44. Center for Yangtze River Delta and Economic Belt Research: Yangtze River Delta Agricultural Development Overview and Regional Comparison. Available online: https://cyrdebr.sass.org.cn/2020/1120/c5524a99196/page.htm (accessed on 25 November 2021).
45. Pu, J.; Xu, H.; Gu, J.; Ma, Q.; Fang, S.; Zhou, L. Impacts of meteorological factors on atmospheric methane mole fractions in the background area of Yangtze River Delta. *China Environ. Sci.* **2013**, *34*, 835–841. [CrossRef]
46. Kuc, T.; Rozanski, K.; Zimnoch, M.; Necki, J.M.; Korus, A. Anthropogenic emissions of CO_2 and CH_4 in an urban environment. *Appl. Energy* **2003**, *75*, 193–203. [CrossRef]
47. Wei, C.; Wang, M.; Fu, Q.; Dai, C.; Huang, R.; Bao, Q. Temporal characteristics of greenhouse gases (CO_2 and CH_4) in the megacity Shanghai, China: Association with air pollutants and meteorological conditions. *Atmos. Res.* **2020**, *235*, 104759. [CrossRef]
48. Wu, J.; Kong, S.; Wu, F.; Cheng, Y.; Zheng, S.; Yan, Q.; Zheng, H.; Yang, G.; Zheng, M.; Liu, D.; et al. Estimating the open biomass burning emissions in central and eastern China from 2003 to 2015 based on satellite observation. *Atmos. Chem. Phys.* **2018**, *18*, 11623–11646. [CrossRef]
49. Yang, Y.; Zhao, Y. Quantification and evaluation of atmospheric pollutant emissions from open biomass burning with multiple methods: A case study for the Yangtze River Delta region, China. *Atmos. Chem. Phys.* **2019**, *19*, 327–348. [CrossRef]
50. National Bureau of Statistics of China: China Statistic Yearbook. Available online: http://www.stats.gov.cn/sj/ndsj/2021/indexch.htm (accessed on 25 June 2022).
51. Pu, J.; Xu, H.; He, J.; Fang, S.; Zhou, L. Estimation of regional background concentration of CO_2 at Lin'an Station in Yangtze River Delta, China. *Atmos. Environ.* **2014**, *94*, 402–408. [CrossRef]
52. Zhu, X.; Zou, J.; Feng, C. Analysis of industrial energy-related CO_2 emissions and the reduction potential of cities in the Yangtze River Delta region. *J. Clean. Prod.* **2017**, *168*, 791–802. [CrossRef]
53. Peng, X.; Lin, X.; Fang, J.; Wang, T.; Jiang, X. Analysis on Coastline and Coastal Wetland Changes in the Hangzhou Bay in Recent 30 Years. *J. Ocean Tech.* **2020**, *39*, 4. [CrossRef]
54. Xiong, J.; Sheng, X.; Wang, M.; Wu, M.; Shao, X. Comparative study of methane emission in the reclamation-restored wetlands and natural marshes in the Hangzhou Bay coastal wetland. *Ecol. Eng.* **2022**, *175*, 106473. [CrossRef]
55. Xia, L.; Zhang, G.; Zhan, M.; Li, B.; Kong, P. Seasonal variations of atmospheric CH_4 at Jingdezhen station in Central China: Understanding the regional transport and its correlation with CO_2 and CO. *Atmos. Res.* **2020**, *241*, 104982. [CrossRef]
56. Hu, C.; Liu, S.; Wang, Y.; Zhang, M.; Xiao, W.; Wang, W.; Xu, J. Anthropogenic CO_2 emissions from a megacity in the Yangtze River Delta of China. *Environ. Sci. Pollut. Res. Int.* **2018**, *25*, 23157–23169. [CrossRef] [PubMed]
57. Li, J.; Huang, X.; Kwan, M.P.; Yang, H.; Chuai, X. The effect of urbanization on carbon dioxide emissions efficiency in the Yangtze River Delta, China. *J. Clean. Prod.* **2018**, *188*, 38–48. [CrossRef] [PubMed]
58. Huang, X.; Wang, T.; Talbot, R.; Xie, M.; Mao, H.; Li, S.; Zhuang, B.; Yang, X.; Fu, C.; Zhu, J.; et al. Temporal characteristics of atmospheric CO_2 in urban Nanjing, China. *Atmos. Res.* **2015**, *153*, 437–450. [CrossRef]
59. WMO World Data Centre for Greenhouse Gases (WDCGG) Data Summary: Greenhouse Gases and Other Atmospheric Gases, No. 44. Japan Meteorological Agency. Available online: https://gaw.kishou.go.jp/static/publications/summary/sum44/sum44.pdf (accessed on 23 June 2022).
60. Zhang, D.; Tang, J.; Shi, G.; Nakazawa, T.; Aoki, S.; Sugawara, S.; Wen, M.; Morimoto, S.; Patra, P.; Hayasaka, T.; et al. Temporal and spatial variations of the atmospheric CO_2 concentration in China. *Geophys. Res. Lett.* **2008**, *35*, L03801. [CrossRef]

61. Zhang, Y.; Jin, J.; Yan, P.; Tang, J.; Fang, S.; Lin, W.; Lou, M.; Liang, M.; Zhou, Q.; Jing, J.; et al. Long-term variations of major atmospheric compositions observed at the background stations in three key areas of China. *Adv. Clim. Chang. Res.* **2020**, *11*, 370–380. [CrossRef]
62. Cheng, S.; Zhou, L.; Tans, P.; An, X.; Liu, Y. Comparison of atmospheric CO_2 mole fractions and source–sink characteristics at four WMO/GAW stations in China. *Atmos. Environ.* **2018**, *180*, 216–225. [CrossRef]
63. Fang, S.; Zhou, L.; Tans, P.; Ciais, P.; Steinbacher, M.; Xu, L.; Luan, T. In situ measurement of atmospheric CO_2 at the four WMO/GAW stations in China. *Atmos. Chem. Phys.* **2014**, *14*, 2541–2554. [CrossRef]
64. Carbon Emission Accounts and Datasets (CEADs): Emission Inventories for 30 Provinces 2019. Available online: https://www.ceads.net/data/province/ (accessed on 25 November 2021).
65. Xia, L.; Zhou, L.; Tans, P.; Liu, L.; Zhang, G.; Wang, H.; Luan, T. Atmospheric CO_2 and its $\delta^{13}C$ measurements from flask sampling at Lin'an regional background station in China. *Atmos. Environ.* **2015**, *117*, 220–226. [CrossRef]
66. Tiemoko, T.D.; Ramonet, M.; Yoroba, F.; Kouassi, K.B.; Kouadio, K.; Kazan, V.; Kaiser, C.; Truong, F.; Vuillemin, C.; Delmotte, M.; et al. Analysis of the temporal variability of CO_2, CH_4 and CO concentrations at Lamto, West Africa. *Tellus B Chem. Phys. Meteorol.* **2020**, *73*, 1–24. [CrossRef]
67. Nguyen, L.N.T.; Meijer, H.A.J.; van Leeuwen, C.; Kers, B.A.M.; Scheeren, H.A.; Jones, A.E.; Brough, N.; Barningham, T.; Pickers, P.A.; Manning, A.C.; et al. Two decades of flask observations of atmospheric $\delta(O_2/N_2)$, CO_2, and APO at stations Lutjewad (the Netherlands) and Mace Head (Ireland), and 3 years from Halley station (Antarctica). *Earth Syst. Sci. Data* **2022**, *14*, 991–1014. [CrossRef]
68. Guo, M.; Fang, S.; Liu, S.; Liang, M.; Wu, H.; Yang, L.; Li, Z.; Liu, P.; Zhang, F. Comparison of atmospheric CO_2, CH_4, and CO at two stations in the Tibetan Plateau of China. *Earth Space Sci.* **2020**, *7*, e2019EA001051. [CrossRef]
69. Shi, X.; Brasseur, G.P. The Response in Air Quality to the Reduction of Chinese Economic Activities during the COVID-19 Outbreak. *Geophys. Res. Lett.* **2020**, *47*, e2020GL088070. [CrossRef] [PubMed]
70. Zambrano-Monserrate, M.A.; Ruano, M.A.; Sanchez-Alcalde, L. Indirect effects of COVID-19 on the environment. *Sci. Total Environ.* **2020**, *728*, 138813. [CrossRef] [PubMed]
71. Xu, J.; Li, X.; Xiao, W.; Ciren, W.; Wen, X.; Liu, S.; Du, X.; Cao, C. ^{13}C-based sources partitioning of atmospheric CO_2 during Youth Olympic Games, Nanjing. *China Environ. Sci.* **2016**, *37*, 4514–4523. [CrossRef]
72. Hu, C.; Liu, C.; Hu, N.; Hong, J.; Ai, X. Government environmental control measures on CO_2 emission during the 2014 Youth Olympic Games in Nanjing: Perspectives from a top-down approach. *J. Environ. Sci.* **2022**, *113*, 165–178. [CrossRef] [PubMed]
73. Pu, J.; Xu, H.; Jiang, Y.; Du, R.; Qi, B. Characteristics of an factors affecting atmospheric CO_2 concentration in Hangzhou. *China Environ. Sci.* **2018**, *39*, 3082–3089. [CrossRef]
74. Tohjima, Y.; Patra, P.K.; Niwa, Y.; Mukai, H.; Sasakawa, M.; Machida, T. Detection of fossil-fuel CO_2 plummet in China due to COVID-19 by observation at Hateruma. *Sci. Rep.* **2020**, *10*, 18688. [CrossRef]
75. Liu, C.; Huang, Z.; Huang, J.; Liang, C.; Ding, L.; Lian, X.; Liu, X.; Zhang, L.; Wang, D. Comparison of $PM_{2.5}$ and CO_2 Concentrations in Large Cities of China during the COVID-19 Lockdown. *Adv. Atmos. Sci.* **2022**, *39*, 861–875. [CrossRef]
76. Wu, Y.; Yang, Z.; Lin, B.; Liu, H.; Wang, R.; Zhou, B.; Hao, J.M. Energy consumption and CO_2 emission impacts of vehicle electrification in three developed regions of China. *Energy Policy.* **2012**, *48*, 537–550. [CrossRef]
77. Xu, X.; Tan, Y.; Chen, S.; Yang, G.; Su, W.Z. Urban household carbon emission and contributing factors in the Yangtze River Delta, China. *PLoS ONE* **2015**, *10*, e0121604. [CrossRef] [PubMed]
78. Xu, X.; Yang, G.; Tan, Y.; Zhuang, Q.; Tang, X.; Zhao, K.; Wang, S. Factors influencing industrial carbon emissions and strategies for carbon mitigation in the Yangtze River Delta of China. *J. Clean. Prod.* **2017**, *142*, 3607–3616. [CrossRef]
79. Liu, Z.; Chen, X.; Cai, J.; Baležentis, T.; Li, Y. The Impact of "Coal to Gas" Policy on Air Quality: Evidence from Beijing, China. *Energies* **2020**, *13*, 3876. [CrossRef]
80. Da, P.; Tao, L.; Sun, K.; Golston, L.M.; Miller, D.J.; Zhu, T.; Qin, Y.; Zhang, Y.; Mauzerall, D.L.; Zondlo, M.A. Methane emissions from natural gas vehicles in China. *Nat. Commun.* **2020**, *11*, 4588. [CrossRef]
81. Rigby, M.; Prinn, R.G.; Fraser, P.J.; Simmonds, P.G.; Langenfelds, R.L.; Huang, J.; Cunnold, D.M.; Steele, L.P.; Krummel, P.B.; Weiss, R.F.; et al. Renewed growth of atmospheric methane. *Geophys. Res. Lett.* **2008**, *35*, L22805. [CrossRef]
82. Turner, A.J.; Frankenberg, C.; Wennberg, P.O.; Jacob, D.J. Ambiguity in the causes for decadal trends in atmospheric methane and hydroxyl. *Proc. Natl. Acad. Sci. USA* **2017**, *114*, 5367–5372. [CrossRef]